Int. J. Solids Structures Vol. 29, No. 9, pp. 1143–1171, 1992
Printed in Great Britain.

0020-7683/92 $5.00 + .00

BIFURCATION AND LOCALIZATION INSTABILITIES IN CYLINDRICAL SHELLS UNDER BENDING—II. PREDICTIONS

G. T. Ju and S. Kyriakides
Engineering Mechanics Research Laboratory, Department of Aerospace Engineering and Engineering Mechanics, The University of Texas at Austin, Austin, TX 78712, U.S.A.

(*Received* 10 *January* 1991; *in revised form* 4 *August* 1991)

Abstract—The second part of this study is concerned with the prediction of the response and various instabilities found in Part I to govern the elastic–plastic flexure of circular cylindrical shells. Sanders' shell kinematics and the principle of virtual work were used to formulate the problem. A Rayleigh–Ritz procedure was used to discretize the problem. The resultant non-linear equations were solved iteratively using Newton's method. The three types of behavior involving bifurcation into short wavelength ripples, localization following the attainment of a natural limit load and interaction of the two were studied. In each case the predicted response was found to be in very good agreement with the experimental result.

NOMENCLATURE

$a_{\alpha\beta}$	metric tensor components
$a_i, a_{ik}, \bar{a}_i$	imperfection amplitudes
$b_{\alpha\beta}$	curvature tensor components
$E_{\alpha\beta}, K_{\alpha\beta}$	membrane and bending strains on shell middle surface
$M_{\alpha\beta}, N_{\alpha\beta}$	moment and stress resultants
R	shell radius
$\{s, z, \theta\}$	co-ordinates
$\{u, v, w\}$	displacements
$\hat{\mathbf{u}}$	bifurcation mode
$\bar{w}(s, \theta)$	initial imperfection
Φ^*	angle of rotation at $s = L$
Φ_l^*	value of Φ^* at limit moment.

INTRODUCTION

This part of the study is concerned with the prediction of the response and instabilities in long shells under pure bending. Of particular interest are shells with lower diameter-to-thickness ratios ($D/t < 100$ for common structural metals) whose behavior is strongly influenced by the plastic characteristics of the material. The experiments presented in Part I, in which aluminum 6061-T6 shells were used, demonstrated that the major deformation characteristic of the response of such shells is the ovalization induced by the bending of their cross-sections. The reduction in rigidity caused by ovalization, combined with the reduction in the modulus of the material as it goes further into the plastic range, lead to a limit moment in the response (*natural limit load instability*). Thus, the first requirement from an analysis of the problem is the capability of predicting accurately the uniform ovalization induced by bending.

In the case of thinner shells, short wavelength rippling followed by catastrophic collapse precede the natural limit load. The collapse is local in nature and is characterized by a number of "diamond" shapes as shown in Fig. 1a for $D/t = 44$ (such buckling modes are common to thin elastic shells). The wavelength of the ripples is only a small fraction of the diameter of the shell. The onset of the rippling can be established by the customary linearized bifurcation criterion [see, for example, Bushnell (1981)^I and Ju and Kyriakides (1990)^I].† The study of the post-buckling behavior of a rippled shell and of the mechanism of collapse will require an analysis which allows the development, growth and possible localization of such ripples.

† ( )^I refers to items from Part I.

As the shell $D\ t$ is reduced, the ripples occur at progressively higher curvatures, which get progressively closer to the curvatures corresponding to the natural limit loads. The collapse mode is now characterized by one sharp local kink, as shown in Fig. 1b. For even thicker shells, a limit load instability is recorded first. In the neighborhood of the limit load, the shell ovalization ceases to be uniform. The deformation localizes in a region a "few" diameters long at a dropping moment. The shell collapses catastrophically by developing a kink, as shown in Fig. 1c, in the trough of localization.

The same behavior was observed for thicker shells. However, such shells retain significant post-limit load strength and collapse becomes progressively less abrupt (see Fig. 1d).

Prediction of localization associated with the natural limit load requires analyzing a shell which is a number of diameters long. Thus, the problem has at least two characteristic axial wavelengths which can differ by one to two orders of magnitude. Clearly this can be expected to complicate numerical discretization schemes. This task is further complicated by the experimental observation that, for shells with intermediate D/t values, the two modes of instability interact and, as a result, the analysis must have the flexibility of addressing this interaction.

A special purpose shell analysis, capable of addressing the characteristics of the problem outlined, has been developed. The primary objectives of the study were to evaluate the pre-buckling response of the shells, identify the dominant instabilities, the initial post-buckling behavior of the shells and, ultimately, the major factors which influence the onset of these instabilities. These goals can be achieved, by and large, within the limitations of Sanders' (1963)[1] non-linear shell equations, which were adopted in the formulation. The validity of the formulation will be verified by direct comparison to the experimental results. The results will be used, in combination with the experimental observations, to illuminate the phenomena described in Part I.

PROBLEM FORMULATION

(1) *Kinematics*

From above the major requirements for the formulation are as follows:

(a) It should be capable of modelling the ovalization of the cross-section.
(b) It should be capable of simulating the growth of short wavelength axial ripples on the compressed side of the shell.
(c) It should allow the deformation of the shell to localize over sections a few diameters long, as observed in the experiments.

In view of the axial length of the localized deformation recorded in the experiments, Sanders' non-linear shell kinematics will be used (mid-surface strains are assumed to be small; rotations of normals to the mid-surface are assumed to be small but finite).

We consider a shell of radius R, wall thickness t and half length L. Points on the shell mid-surface are identified by (θ, s) (see Fig. 2a). The plane $s = 0$ is assumed to be a plane of symmetry. Because the problems of interest have distinctly different length scales, shells in categories (1) and (3) in Part I will be treated separately at first.

For algebraic convenience and easier interpretation of the results, it is desirable that the displacement components be measured from a circular toroidal reference shell (see Fig. 2b). To achieve this, we deform the shell in steps and use a deformation composition scheme similar to the one used by Fabian (1981)[1] to establish the final strains in the shell. The initial (undeformed) circular cylinder can be described through the metric tensor $a^0_{\alpha\beta}$ (fundamental tensor) and the curvature tensor $b^0_{\alpha\beta}$ as follows $[(\alpha, \beta) = 1, 2]$:

$$[a^0_{\alpha\beta}] = \begin{bmatrix} 1 & 0 \\ 0 & 1 \end{bmatrix}, \quad [b^0_{\alpha\beta}] = \begin{bmatrix} 0 & 0 \\ 0 & \dfrac{1}{R} \end{bmatrix}. \tag{1}$$

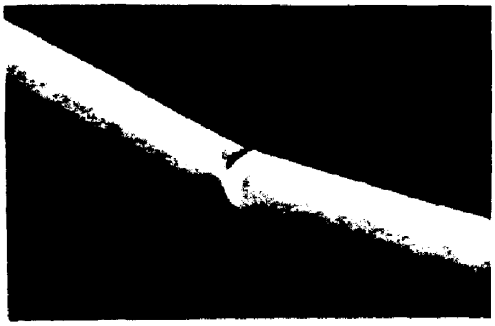

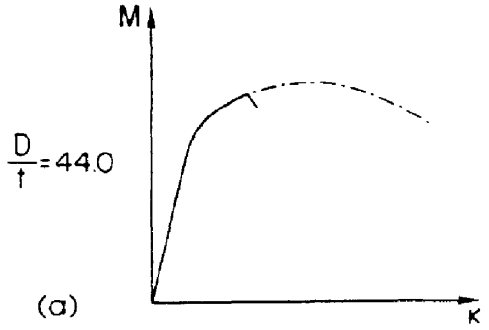

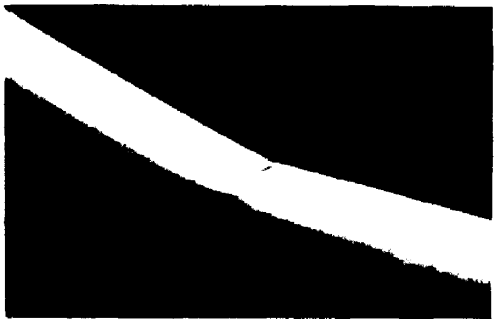

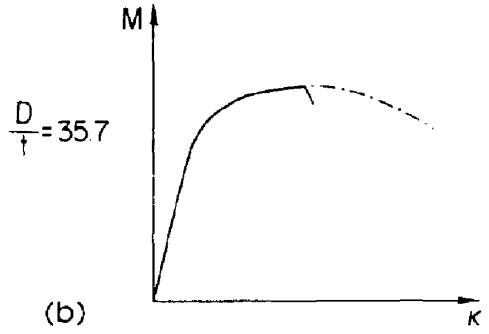

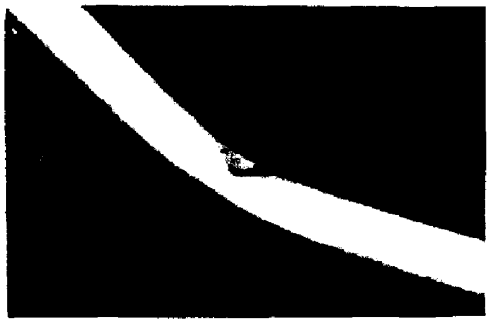

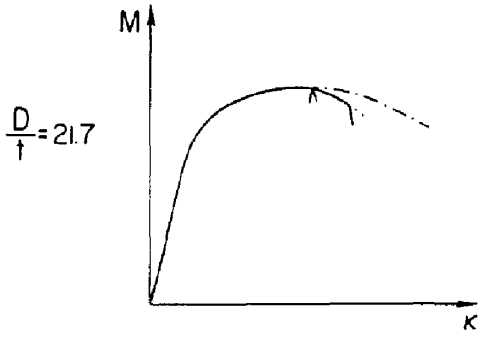

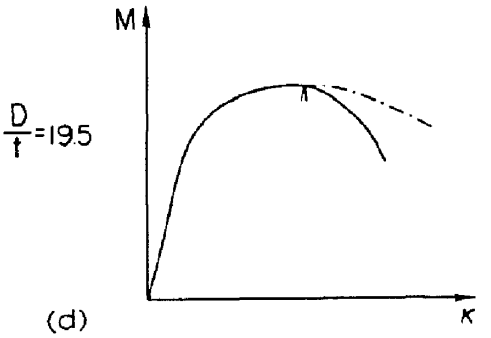

Fig. 1. Buckling modes and corresponding moment–curvature responses of shells of different D/t values.

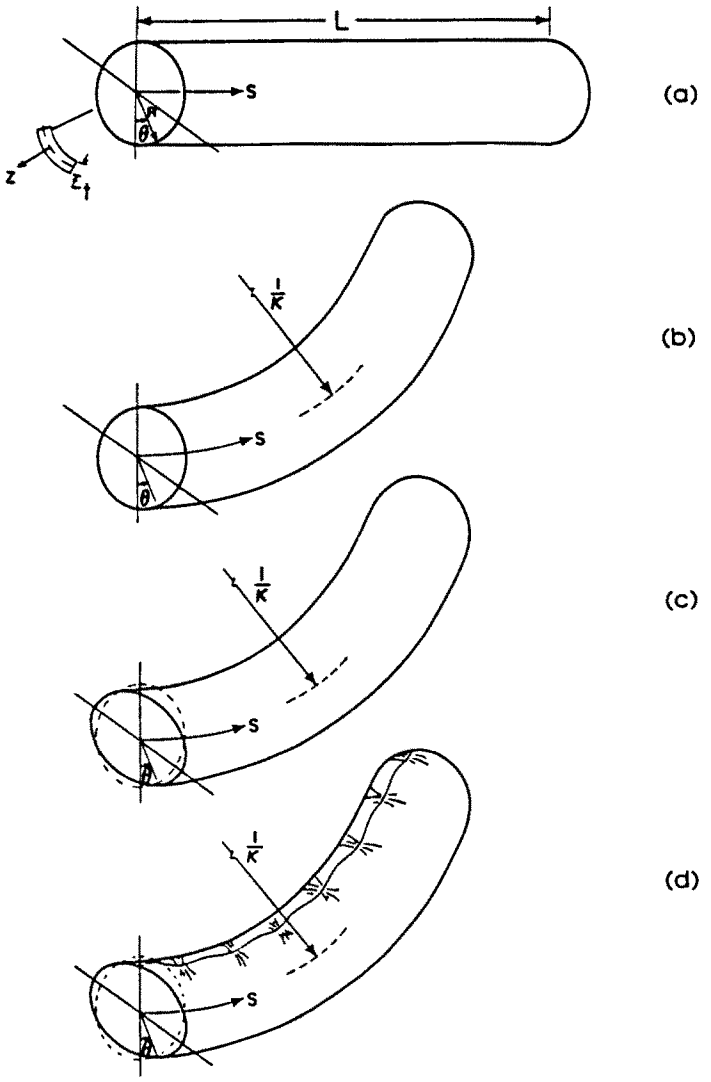

Fig. 2. Configurations of shells analyzed.

The circular torus has metric and curvature tensors given by:

$$[a^1_{\alpha\beta}] = \begin{bmatrix} 1+2\kappa R\cos\theta & 0 \\ 0 & 1 \end{bmatrix}, \quad [b^1_{\alpha\beta}] = \begin{bmatrix} \dfrac{\kappa\cos\theta}{1+\kappa R\cos\theta} & 0 \\ 0 & \dfrac{1}{R} \end{bmatrix} \tag{2}$$

where κ and θ are defined in Fig. 2b. The membrane and bending strains in the torus, $\hat{E}_{\alpha\beta}$ and $\hat{K}_{\alpha\beta}$, are related to (1) and (2) as follows:

$$a^1_{\alpha\beta} = a^0_{\alpha\beta} + 2\hat{E}_{\alpha\beta}, \quad b^1_{\alpha\beta} = b^0_{\alpha\beta} + \hat{K}_{\alpha\beta}. \tag{3}$$

The circular toroidal shell is now allowed to deform further by developing additional displacements $\{u, v, w\}$ in the s, θ and radial directions respectively. The deformed shell is defined by

$$a^2_{\alpha\beta} = a^1_{\alpha\beta} + 2E^*_{\alpha\beta}, \quad b^2_{\alpha\beta} = b^1_{\alpha\beta} + K^*_{\alpha\beta} \tag{4}$$

where $E^*_{\alpha\beta}$ and $K^*_{\alpha\beta}$ are the additional deformations imposed on the circular torus. Their general form is as follows [see Appendix in Sanders (1963)']:

$$E^*_{ss} = \frac{1}{1+\kappa R\cos\theta}[u_{,s} - v\kappa\sin\theta + w\kappa\cos\theta] + \tfrac{1}{2}\phi_1^2 + \tfrac{1}{2}\phi^2,$$

$$E^*_{\theta\theta} = \frac{1}{R}[v_{,\theta} + w] + \tfrac{1}{2}\phi_2^2 + \tfrac{1}{2}\phi^2,$$

$$E^*_{s\theta} = \frac{1}{2(1+\kappa R\cos\theta)}\left[u_{,\theta}\frac{(1+\kappa R\cos\theta)}{R} + v_{,s} + u\kappa\sin\theta\right] + \tfrac{1}{2}\phi_1\phi_2,$$

$$K^*_{ss} = \frac{1}{1+\kappa R\cos\theta}[\phi_{1,s} - \phi_2\kappa\sin\theta],$$

$$K^*_{\theta\theta} = \frac{\phi_{2,\theta}}{R},$$

$$K^*_{s\theta} = \frac{1}{2(1+\kappa R\cos\theta)}\left[\phi_{1,\theta}\frac{(1+\kappa R\cos\theta)}{R} + \phi_{2,s} + \phi_1\kappa\sin\theta + \phi\right],$$

$$\phi_1 = \frac{1}{1+\kappa R\cos\theta}[-w_{,s} + u\kappa\cos\theta],$$

$$\phi_2 = \frac{1}{R}[-w_{,\theta} + v],$$

$$\phi = \frac{1}{2(1+\kappa R\cos\theta)}\left[v_{,s} - u_{,\theta}\frac{(1+\kappa R\cos\theta)}{R} + u\kappa\sin\theta\right]. \tag{5}$$

If the shell deformation is uniform along s (i.e. uniform ovalization as shown in Fig. 2c) then $u = 0$ and $(\ )_{,s} = 0$ in (5); otherwise (5) can be used to describe general deformations (e.g. Fig. 2d). The total deformation is given by

$$E_{\alpha\beta} = \tfrac{1}{2}(a^2_{\alpha\beta} - a^0_{\alpha\beta}) \quad \text{and} \quad K_{\alpha\beta} = (b^2_{\alpha\beta} - b^0_{\alpha\beta}). \tag{6}$$

The strains $\varepsilon_{\alpha\beta}$ at any point in the shell are given by

$$\varepsilon_{\alpha\beta} = (E_{\alpha\beta} + zK_{\alpha\beta})/(A_\alpha A_\beta)^{1/2}, \quad A_1 \simeq 1, \quad A_2 \simeq 1 + \frac{z}{R} \tag{7}$$

[see Bushnell (1974)].

If the shell has initial geometric imperfections then (1) must be altered appropriately, say to $\bar{a}^0_{\alpha\beta}$ and $\bar{b}^0_{\alpha\beta}$ (see Appendix A), and eqn (6) becomes

$$E_{\alpha\beta} = \tfrac{1}{2}[a^2_{\alpha\beta} - \bar{a}^0_{\alpha\beta}], \quad K_{\alpha\beta} = [b^2_{\alpha\beta} - \bar{b}^0_{\alpha\beta}]. \tag{8}$$

(2) *Constitutive equations*

The inelastic material behavior was modelled through the J_2 flow theory of plasticity with isotropic hardening. Under the customary assumption of plane stress, the incremental

constitutive equations reduce to

$$\dot{\varepsilon}_{\alpha\beta} = \frac{1}{E}[(1+\nu)\dot{\sigma}_{\alpha\beta} - \nu\dot{\sigma}_{\gamma\gamma}\delta_{\alpha\beta}] + q s_{\alpha\beta}s_{\gamma\delta}\dot{\sigma}_{\gamma\delta},$$

$$q = \begin{cases} \dfrac{3}{4J_2}\left[\dfrac{1}{E_t} - \dfrac{1}{E}\right], & \dot{J}_2 > 0 \\ 0, & \dot{J}_2 \leqslant 0 \end{cases} \tag{9}$$

where $\mathbf{s} = \boldsymbol{\sigma} - \frac{1}{3}\mathrm{tr}(\boldsymbol{\sigma})\mathbf{I}$, $J_2 = \frac{1}{2}\mathbf{s}\cdot\mathbf{s}$. E is the material Young's modulus, ν the Poisson ratio and E_t is the tangent modulus. In the numerical simulations that follow the uniaxial response was fitted with the Ramberg–Osgood fit (eqn (3)[1]; data given in Table 1[1]) from which

$$\frac{1}{E_t} - \frac{1}{E} = \frac{3}{7}\frac{n}{E}\left(\frac{3J_2}{\sigma_y^2}\right)^{(n-1)/2}. \tag{10}$$

Bifurcation buckling calculations were carried out using the J_2 deformation theory of plasticity which historically has been shown to lead to predictions which are in better agreement with experiments [see Hutchinson (1974)[1]]. The incremental form of the appropriate equations is as follows:

$$\dot{\varepsilon}_{\alpha\beta} = \frac{1}{E_s}[(1+\nu_s)\dot{\sigma}_{\alpha\beta} - \nu_s\dot{\sigma}_{\gamma\gamma}\delta_{\alpha\beta}] + Q s_{\alpha\beta}s_{\gamma\delta}\dot{\sigma}_{\gamma\delta},$$

$$Q = \frac{3}{4J_2}\left[\frac{1}{E_t} - \frac{1}{E_s}\right] \tag{11}$$

where E_s is the secant modulus given by

$$\frac{1}{E_s} - \frac{1}{E} = \frac{3}{7}\frac{1}{E}\left(\frac{3J_2}{\sigma_y^2}\right)^{(n-1)/2}$$

and

$$\nu_s = \frac{1}{2} + \frac{E_s}{E}\left(\nu - \frac{1}{2}\right). \tag{12}$$

The membrane and bending stress resultants (intensities) are obtained by integrating the stresses through the wall thickness as follows:

$$N_{\alpha\beta} = \int_{-t/2}^{t/2} \frac{A_1A_2}{(A_\alpha A_\beta)^{1/2}}\sigma_{\alpha\beta}\,\mathrm{d}z \quad \text{and} \quad M_{\alpha\beta} = \int_{-t/2}^{t/2} \frac{A_1A_2}{(A_\alpha A_\beta)^{1/2}}\sigma_{\alpha\beta}z\,\mathrm{d}z. \tag{13}$$

(3) *Principle of virtual work*

Equilibrium is satisfied through the principle of virtual work (PVW) which can be stated as follows:

$$\int_A \{N_{\alpha\beta}\delta E_{\alpha\beta} + M_{\alpha\beta}\delta K_{\alpha\beta}\}\,\mathrm{d}A = \delta W \tag{14}$$

where A is the surface area of the shell and δW the virtual work of the external forces.

SOLUTION PROCEDURE AND RESULTS

The shell was loaded incrementally by prescribing either the overall curvature κ in eqn (2), or the rotation Φ^* at $s = L$. As a result, δW in eqn (14) is zero. The integrations were performed by Gaussian quadrature. The structure was discretized by adopting suitable expansions for the displacements $\{u, v, w\}$. The expansions adopted for each application are given below.

(1) *Uniform ovalization*

In this case, $(\ )_{,s} = 0$ and $u = 0$ in eqn (5). The following displacement expansions were used [see Gellin (1980)[7] and Shaw and Kyriakides (1985)[1]]:

$$v = R\sum_{n=2}^{N_v} b_n \sin n\theta, \quad w = R\sum_{n=0}^{N_w} a_n \sin n\theta. \tag{15}$$

Typically, $N_v = N_w = 6$ was found to yield sufficiently accurate results. Seven Gaussian integration points through the thickness and 12 in the $\theta \in [0, \pi]$ direction were used. Substituting (15) into (14), the PVW can be restated as follows:

$$\left\{2R\int_0^{\pi} [N_{\alpha\beta}E_{\alpha\beta,i} + M_{\alpha\beta}K_{\alpha\beta,i}]\,\mathrm{d}\theta\right\}\delta q_i = 0$$

$$i = 1, 2, \ldots, N_v + N_w \tag{16}$$

where

$$\mathbf{q} = [a_0, a_1, \ldots, a_{N_w}, b_2, b_3, \ldots, b_{N_v}]^{\mathrm{T}}.$$

For each prescribed value of κ, δ_{q_i} are arbitrary. As a result, eqn (16) yields $(N_v + N_w)$ nonlinear algebraic equations which are solved numerically using the Newton–Raphson method.

The kinematic relations used in the formulation of the problem allow only for moderate rotations of the normals to the mid-surface. In order to test the adequacy of these kinematics, moment–curvature and ovalization–curvature responses calculated for a number of shells were compared with the corresponding results from the solution procedure of Shaw and Kyriakides (1985)[1], which is based on large rotation kinematics. For the aluminum shells used in the experiments, the two sets of results were in very close agreement (e.g. for shell No. 9 in Table 1[1] with $D/t = 25.3$, the two limit curvatures differed by 1.5% and the limit moment by 0.002%). In all cases, the ovalization induced by bending is relatively small due to the influence of inelastic material effects. The rotations are, in general, quite moderate and their influence is relatively small; as a result, the predictions from Sanders' shell equations should be dependable.

A bigger difference between the results from the two formulations was observed in linearly elastic shells. Such shells undergo significant ovalization prior to reaching their limit moment. The rotations of the normals are proportionately larger and the results from the present formulation are somewhat less accurate. For example, in the case of a shell with $D/t = 200$, the limit moment and corresponding curvature predicted by the current formulation were 1.2% and 5% lower than the more accurate results, respectively. In view of the favorable comparison observed in the elastic–plastic cases, and of the simplicity afforded by using this type of kinematics in the analysis, it was concluded that Sanders' kinematics were quite suitable for analyzing the problems of interest to this study.

(2) *Bifurcation analysis*

The possibility of bifurcation buckling from the uniformly ovalized state to one which has periodic waves on the compressed side of the shell was checked through the following procedure. Following Hill (1958)[7] and Hutchinson (1974)[7], it is assumed that, at the

equilibrium state in question, there exist two possible incremental solutions $\mathbf{u}^1$ and $\mathbf{u}^2$ [$\mathbf{u} \equiv (u, v, w)^T$]. We denote their difference by $\{\tilde{}\}$ which we identify as the buckling mode given by

$$\tilde{w} = R\cos ps \sum_{n=0}^{N_w} C_n \cos n\theta,$$

$$\tilde{v} = R\cos ps \sum_{n=1}^{N_v} D_n \sin n\theta,$$

$$\tilde{u} = R\sin ps \sum_{n=0}^{N_u} E_n \cos n\theta \tag{17}$$

where $\tilde{\mathbf{u}}$ are measured from the same circular, toroidal reference shell used in the rest of the formulation. Clearly, $\{\tilde{}\}$ must satisfy the PVW and, as a result

$$\left\{R\int_0^{s'}\int_0^{\pi} [N_{\alpha\beta,j}E_{\alpha\beta,i} + M_{\alpha\beta,j}K_{\alpha\beta,i} + N^0_{ss}E_{ss,ij} + N^0_{\theta\theta}E_{\theta\theta,ij}]\,ds\,d\theta\right\}\tilde{q}_i\tilde{q}_j = 0$$

$$i, j = 1, 2, \ldots, (\tilde{N}_w + \tilde{N}_v + \tilde{N}_u + 2) \tag{18}$$

where

$$\lambda = \frac{\pi}{p}, \quad \tilde{\mathbf{q}} = [C_0, C_1, \ldots, C_{N_w}, D_1, \ldots, D_{N_v}, E_0, E_1, \ldots, E_{N_u}]^T$$

and $\mathbf{N}^0$ are the membrane stresses from the pre-buckling solution presented in the previous section. In abbreviated form, eqn (18) can be expressed as

$$\tilde{\mathbf{q}}^T\mathbf{H}\tilde{\mathbf{q}} = 0. \tag{19}$$

If the solution tested is unique, then $\mathbf{H}$ is positive definite. At the point of bifurcation, $\det \mathbf{H} = 0$. Typically, the $\det \mathbf{H}$ is evaluated at every loading increment of the pre-buckling solution procedure using Hill's concept of a comparison solid (yields lower bound estimates of the bifurcation loads). In evaluating $\mathbf{H}$, the J_2 deformation theory of plasticity was used to calculate the instantaneous moduli of the material. A trial value of $p = \pi/\lambda_c$ (λ_c given in eqn (8)[7]) was used. Once a change in sign was identified, p and the curvature κ were varied until the critical values λ_b and κ_b were found to a sufficient accuracy.

Bifurcation buckling analyses and results have been presented by a number of previous investigators. Wherever possible, published results were compared with predictions from the present formulation. For example, Stephens *et al.* (1975)[7] used the STAGS program to analyze elastic shells of finite length under pure bending. The critical moment of the longer shell they analyzed was found to be in good agreement with the present predictions. Fabian carried out a detailed analysis of long elastic shells. His calculations for a shell with $D/t = 120$ were repeated. The critical moment, curvature and wavelength were found to be in very good agreement with the predictions from the present analysis (difference less than 3%).

Plastic bifurcation calculations have been conducted by Bushnell (1980)[7] using his BOSOR-5 axisymmetric shell analysis. An example from this work involving an elastic–perfectly plastic shell with $D/t = 55.3$ was analyzed with the present formulation by approximating the material with a Ramberg–Osgood fit with $n = 200$. The critical moment and curvature were found to be in excellent agreement with Bushnell's predictions, but the critical wavelengths differed due to the approximation made in the stress–strain response. Gellin (1976), developed an approximate plastic bifurcation analysis using the DMV shell equations for cylindrical shells and the pre-buckling stress state from his long tube analysis (1980)[7]. The results presented in Table 2 of his paper were recalculated with the present

formulation. Good agreement was found for the thickest ($D/t = 60$) of the shells analyzed (critical curvature 1.7% higher than Gellin's). In the case of the shell with $D/t = 200$ the critical curvature predicted by the present formulation was approximately 4% lower than his prediction.

Figures 3 and 4 show comparisons of the predicted and measured moment–curvature and ovalization–curvature responses for shells with $D/t = 50$ and 44, respectively. These shells developed axial ripples prior to the natural limit load instability. The measured and predicted bifurcation points and values are identified on the respective responses [(↑) ≡ predicted bifurcation; (↓) ≡ ripples first detected in experiment]. The predictions of the responses as well as of the bifurcation points are seen to be in very good agreement with the experimental results.

Very good agreement between experiments and predictions was obtained for all the shells tested which exhibited bifurcation buckling as demonstrated in Fig. 23[1]. An area of disagreement between experiment and analysis is shown in Fig. 5, where the critical half wavelengths yielded by the analysis (λ_D) are compared to the experimental values (λ_{exp}) for shells with $20 < D/t < 55$. The predicted wavelengths are uniformly longer than those measured in the experiments. Similar bifurcation calculations, based on the J_2 flow theory of plasticity, yielded unrealistically high values of critical curvatures and even longer values of critical λ [consistent with results in other plastic buckling problems—see Batdorf (1949)]. In view of this, the corner theory of plasticity [see Christoffersen and Hutchinson (1979)] can be expected to also yield wavelengths which are longer than λ_D. This discrepancy is confirmed by similar measurements made by Reddy in his experimental study of the problem of 1979[1]. He compared his measurements with predictions for axially loaded cylinders [eqn (8)[1]] and found a similar difference between experiment and analysis. Figure 6 shows a comparison of λ_D, obtained from the current bending analysis, to the critical wavelength of axially loaded cylinders of various D/ts (the average material properties of the aluminum

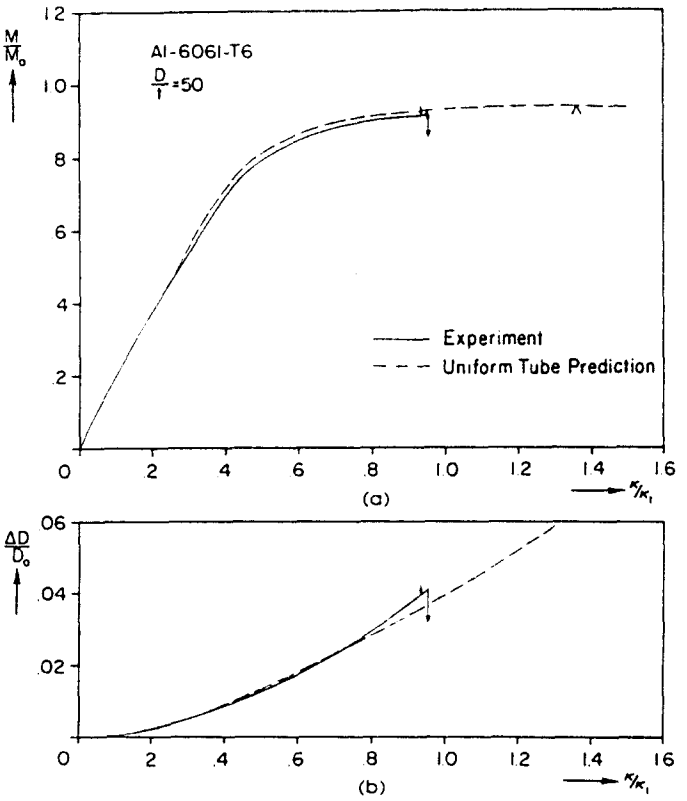

Fig. 3. Bending response of aluminum shell with $D/t = 50$: (a) moment–curvature; (b) ovalization–curvature. [(A) ≡ limit moment; bifurcation: experiment (↓), predicted (↑).]

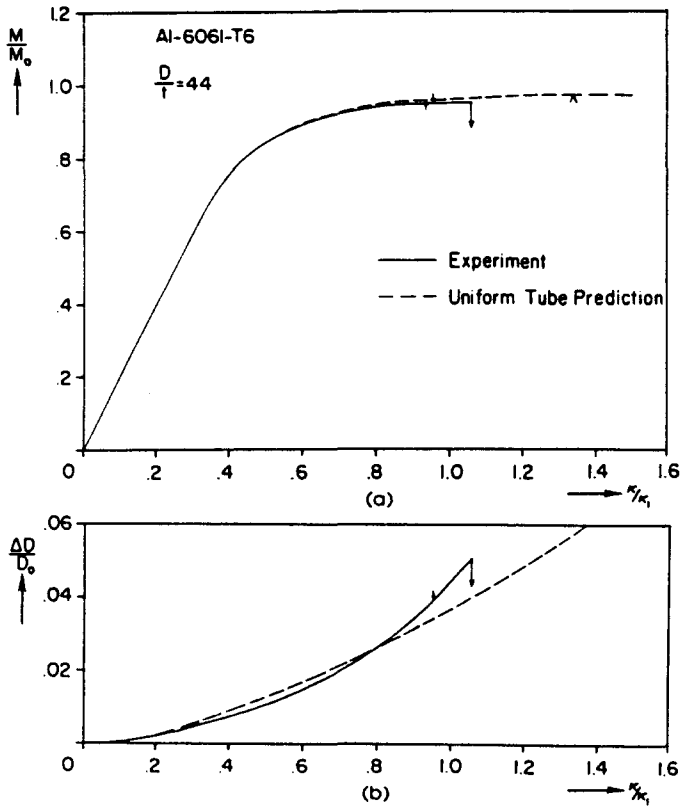

Fig. 4. Bending response of aluminum shell with $D/t = 44$: (a) moment–curvature; (b) ovalization–curvature.

shells tested, given in Part I, were used). It is interesting to observe that the critical wavelengths of the two problems do not differ significantly. The value corresponding to axisymmetric buckling of axially loaded elastic cylinders, λ_E is also included. Even this value compares quite well with the other values for the whole range of D/t of interest here.

We, thus, conclude that Reddy's results are very similar to ours and that a discrepancy between experiment and analysis regarding the critical wavelengths, λ_c, does exist. The reason for this discrepancy is not known at this time. However, in spite of this difference, the more important quantity of critical curvature, κ_b, yielded by this analysis, was consistently found to be in very good agreement with the experimental results.

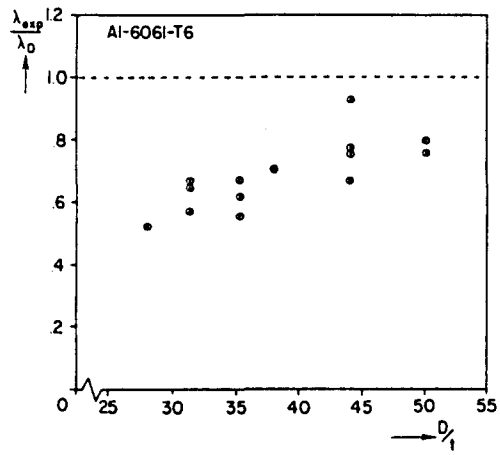

Fig. 5. Comparison between measured and predicted axial ripple wavelengths as a function of D/t.

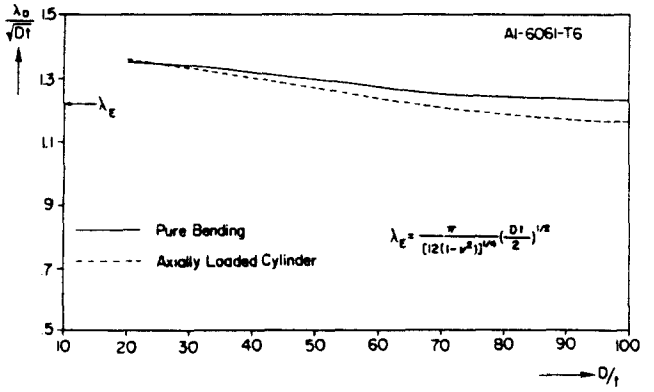

Fig. 6. Predicted λ_D as a function of D/t for axially loaded cylinder and cylinder in pure bending (λ_E corresponds to elastic, axially loaded cylinder).

(3) *Post-buckling behavior and effect of imperfections*

The post-buckling behavior of the shell can be analyzed by allowing for deformations which vary along the length of the shell. A first step in such an effort is to consider a shell with initial geometric imperfections which are related to the critical buckling mode obtained from the bifurcation analysis presented above. We thus consider a circular cylindrical shell with axisymmetric imperfections defined as follows:

$$\bar{w} = -a_{0i} R \cos \frac{\pi s}{\lambda_D} \tag{20}$$

where λ_D is the critical wavelength of the ripples calculated from the bifurcation analysis. (A similar study was conducted by Fabian (1981)[1] but in eqn (20) instead of λ_D, he used λ_c (eqn (8)[1]) obtained from axially-loaded elastic shells.) If it is assumed that the axial ripples grow uniformly along the shell length, then it is sufficient to analyze a shell with $L = \lambda_D$. In this case, the complete strain–displacement equations given in eqn (5) are used with the following expansions for the displacements:

$$\begin{aligned} u &= R \sum_{i=1}^{I_u} \sum_{j=0}^{J_u} c_{ij} \sin ips \cos j\theta, \\ v &= R \sum_{n=2}^{N_v} b_n \sin n\theta + R \sum_{i=1}^{I_v} \sum_{j=1}^{J_v} d_{ij} \cos ips \sin j\theta, \\ w &= R \sum_{n=0}^{N_w} a_n \cos n\theta + R \sum_{i=1}^{I_w} \sum_{j=0}^{J_w} e_{ij} \cos ips \cos j\theta, \end{aligned} \tag{21}$$

where $p = \pi/\lambda_D$. Typical values for the number of terms found to be sufficient were $N_v = N_w = J_u = 6$ and $I_u = 4$.

The first case analyzed was a linearly elastic shell with the following characteristics: $D = 1.250$, $D/t = 200$, $\nu = 0.32$. The critical moment and curvature values predicted for the perfect case are as follows:

$$\begin{aligned} \kappa_b/\kappa_1 &= 1.74, \qquad \kappa_L/\kappa_1 = 1.95, \\ M_b/M^* &= 0.924, \quad M_L/M^* = 0.935, \\ \lambda_E/\sqrt{Dt} &= 1.693, \end{aligned}$$

where $M^* = ERt^2/(1-\nu^2)$ and λ_E is the half wavelength of the axial ripple bifurcation mode. In the imperfect cases, λ_D was replaced by λ_E in eqns (20, 21). The moment–curvature and ovalization–curvature responses for imperfection amplitudes of $a_{0i} = 0$, 10^{-4} and 3×10^{-4}

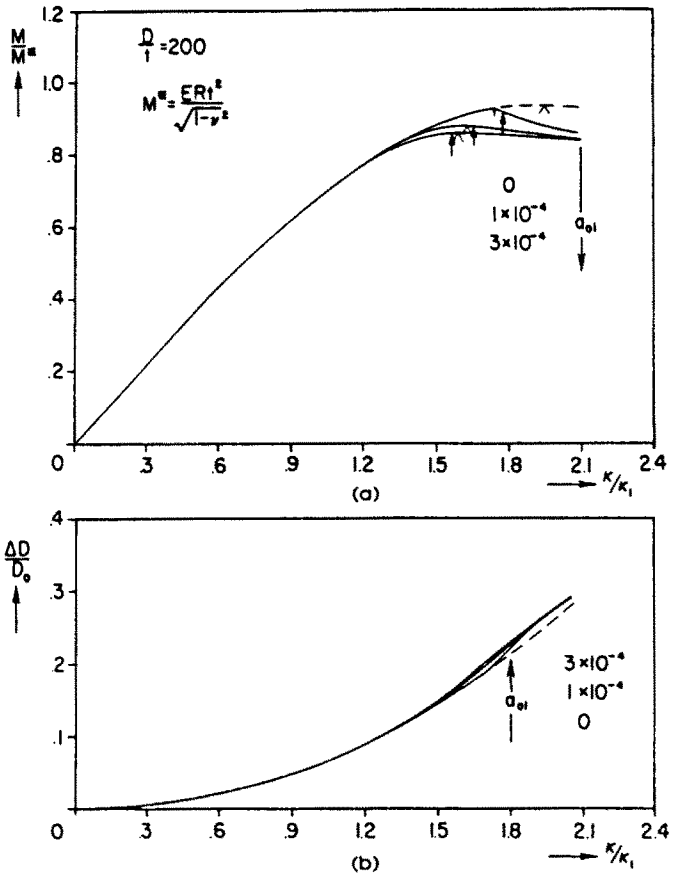

Fig. 7. Predicted bending response of perfect and imperfect elastic shell: (a) moment curvature; (b) ovalization curvature.

are shown in Fig. 7 (ovalization in the valley of imperfection). As observed by previous investigators [Axelrad (1980)'; Fabian (1977)'; Gellin (1980)'] bifurcation buckling precedes the limit load instability. The post-buckling response has a distinctly negative slope. This leads to the expectation that longer shells will experience localized deformation following bifurcation buckling. The presence of axial imperfections leads to a limit load instability which occurs at reduced values of moment and curvature, as shown in the figure.

A similar study of the effect of axisymmetric imperfections on elastic–plastic shells was conducted on an aluminum shell with $D/t = 44$ (see Table 1') which is representative of the thinner group of shells studied experimentally. The results are shown in Fig. 8. The main influence of the imperfections on the calculated responses is seen to occur once the shell enters the plastic range of the material. Due to the imperfections the shell becomes more compliant and the limit load instability occurs at a smaller curvature than that of the perfect shell. The value of κ_L is seen to become progressively reduced as the imperfection amplitude is increased. Figure 9 shows a graphical reproduction of a calculated equilibrium state of this shell which uniformly distributed axial ripples (generated on an image processing system consisting of a Grinnell 270 display system coupled with a microVAX II-MOVIE.BYU data processing system).

(4) *Second bifurcation*

In the experimental part of the study it was observed that the thinner shells tested ($D/t > 44$) developed ripples at an increasing load. Soon after the appearance of the ripples the shell collapsed by developing one sharp local buckle characterized by a number of circumferential waves as evidenced by the diamond nature of the collapse mode shown in Fig. 1a. This sequence of events is reminiscent of the behavior observed in the related

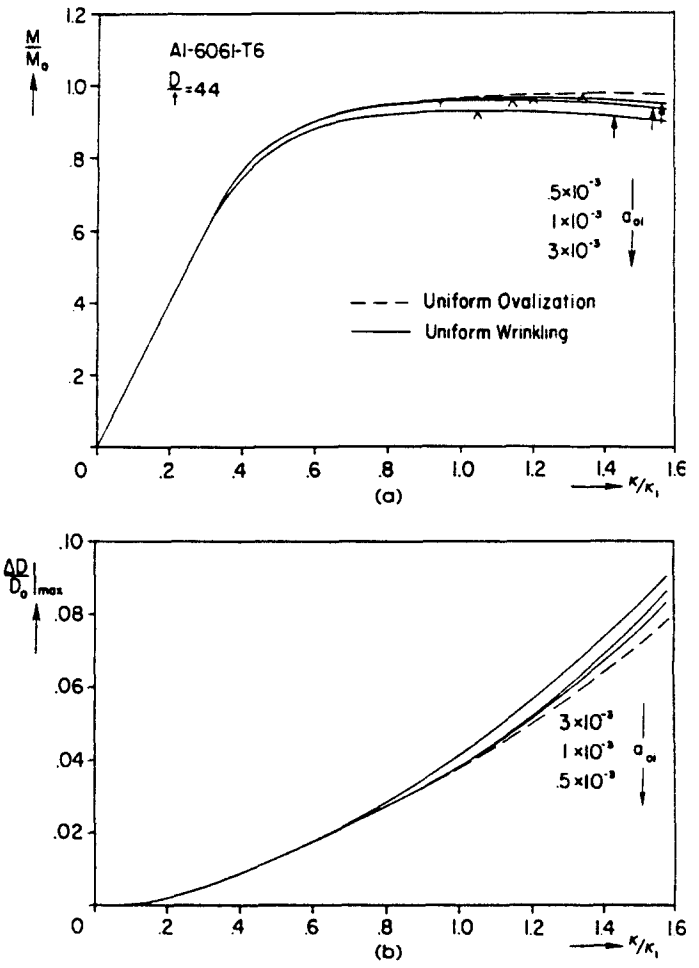

Fig. 8. Calculated responses for shells with initial axisymmetric imperfections: (a) moment–curvature; (b) ovalization–curvature. [(↑) ≡ first bifurcation; (↑) ≡ second bifurcation.]

problem of plastic buckling of axial loaded cylindrical shells [see Lee (1962)', Gellin (1976), Tvergaard (1983)' and Yun and Kyriakides (1990)']. Motivated by the experimental observations and the works on this related problem we developed an analysis for bifurcation from the uniformly rippled state to one involving the following buckling mode:

$$\begin{aligned}
\tilde{w} &= R\sum_{i=1}^{I_w}\sum_{j=0}^{J_w} A_{ij}\cos(i-\tfrac{1}{2})ps\cos j\theta,\\
\tilde{v} &= R\sum_{i=1}^{I_v}\sum_{j=1}^{J_v} B_{ij}\cos(i-\tfrac{1}{2})ps\sin j\theta,\\
\tilde{u} &= R\sum_{i=1}^{I_u}\sum_{j=0}^{J_u} C_{ij}\sin(i-\tfrac{1}{2})ps\cos j\theta
\end{aligned} \tag{22}$$

where $p = \pi/\lambda_D$ [i.e. it is assumed that the axial wavelength of this buckling mode is twice that of the first one—see Koiter (1963) and Gellin (1976)].

Using the same arguments as before the bifurcation check is again

$$\tilde{\mathbf{q}}^{\mathrm{T}}\mathbf{H}\tilde{\mathbf{q}} = 0$$

where

$$\mathbf{H} = \int_{-\lambda_D}^{\lambda_D}\int_0^{\pi}\{N_{\alpha\beta,j}E_{\alpha\beta,i} + M_{\alpha\beta,j}K_{\alpha\beta,i} + N^0_{ss}E_{ss,ij} + N^0_{\theta\theta}E_{\theta\theta,ij} + N^0_{s\theta}E_{s\theta,ij}\}\,\mathrm{d}\theta\,\mathrm{d}s \tag{23}$$

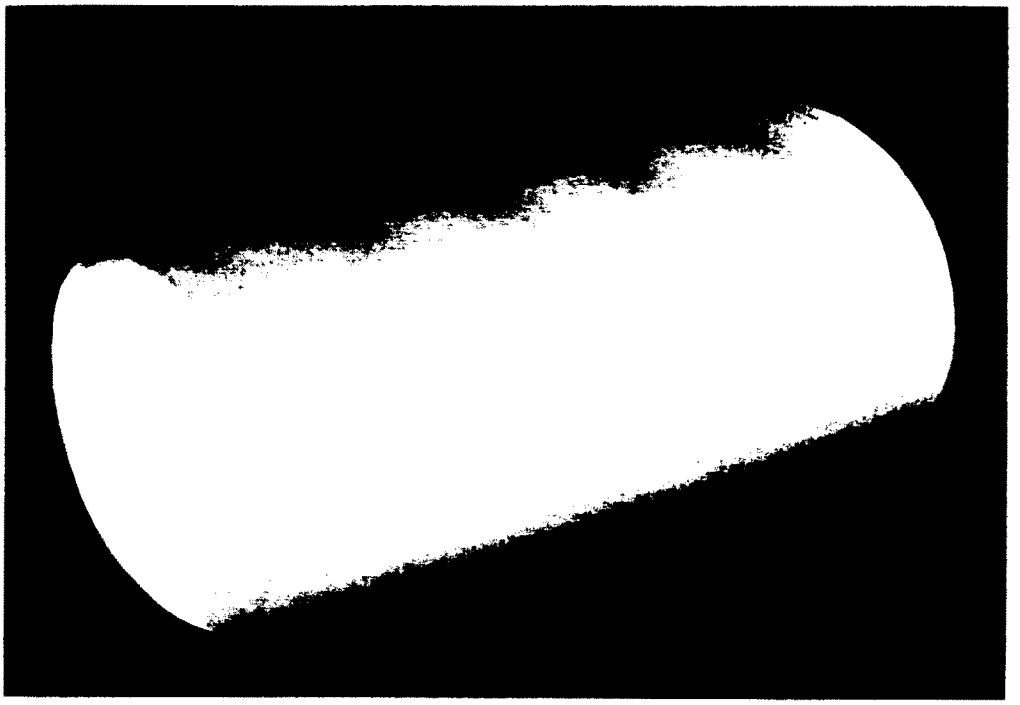

Fig. 9. Graphical reproduction of calculated deformed configuration of shell exhibiting axial ripples (w amplified $\times 2$; $D/t = 44$).

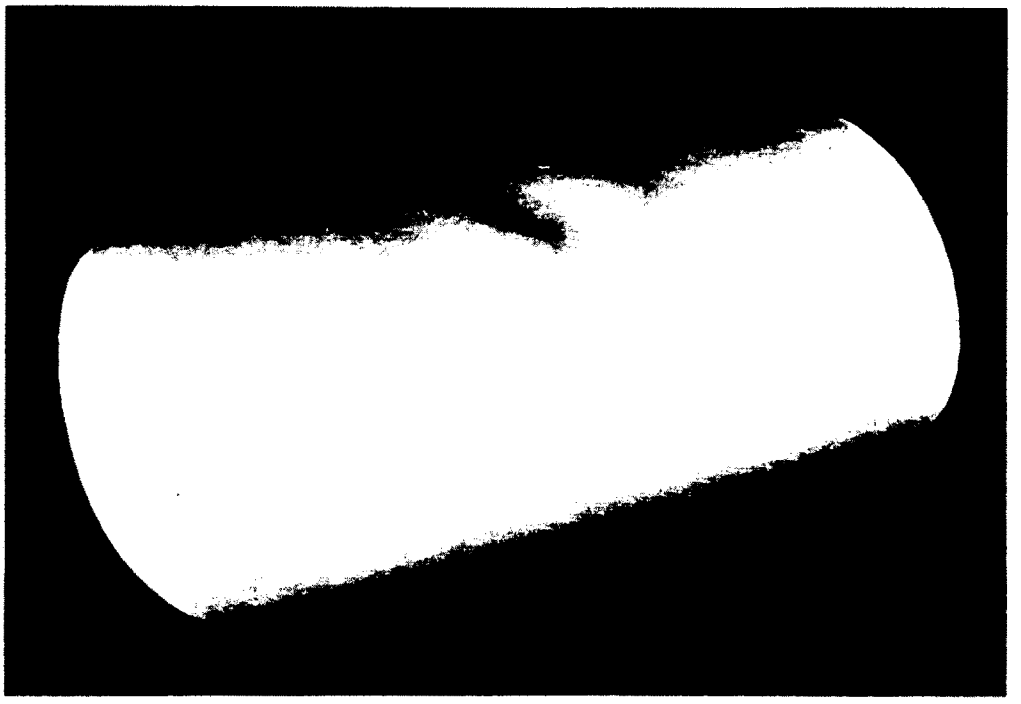

Fig. 13. Graphical reproduction of calculated deformed configuration of shell exhibiting localization of axial ripples ($D/t = 44$).

Fig. 18. Graphical reproduction of calculated deformed shell configuration illustrating localization (D/t = 19.5).

and

$$\tilde{\mathbf{q}} = [A_{10}, \ldots, A_{I_a J_a}, B_{11}, B_{12}, \ldots, B_{I_b J_b}, C_{10}, C_{11}, \ldots, C_{I_a J_a}]^{\mathrm{T}}.$$

Bifurcation points calculated using this procedure are identified with a bold (↑) in Figs 7 and 8. In the case of the elastic shell the second bifurcation is found to occur either soon after the limit load or just prior to it. In the elastic–plastic case shown in Fig. 8, the second bifurcation occurs at a curvature which is significantly larger than that corresponding to the limit load. These critical values are significantly higher than the curvature at which the shell collapsed and as a result it is concluded that an alternative mechanism must be responsible for the catastrophic collapse of the shell.

(5) *Localization of axial waves*

From the results presented so far, it has been demonstrated that at some curvature the shell can develop uniform axial ripples. As a result, the overall stiffness of the shell is reduced and a limit load develops (earlier than the natural limit load). It has been shown [see Tvergaard and Needleman (1980), Needleman and Tvergaard (1982) and Tvergaard (1983)] that structures which exhibit such behavior tend to develop localized buckling patterns soon after the limit load. This behavior was indeed observed in the experiments conducted. The possibility of this occurring will be checked by considering a section of a shell containing a number of axial ripples ($L = 5\lambda_p$). A small initial imperfection, $\bar{w}(s)$, is included which provides a small bias to the amplitude of one of the ripples. The imperfection is given by

$$\bar{w} = -R\left[a_{0_i} + a_i \cos\left(\frac{\pi s}{5\lambda_p}\right)\right]\cos\left(\frac{\pi s}{\lambda_p}\right). \tag{24}$$

The displacement expansions adopted are similar to those in eqn (21) with $p = \pi/5\lambda_p$ and $I_a = 6$, $J_a = 8$ (45 integration points were used in the axial direction).

The ripples were found to localize. The effect of localization on the response is shown in Fig. 10, where results from the uniform ovalization analysis, the uniform ripple analysis and the localized ripple analysis are compared. As observed earlier, axial ripples have a "softening" effect on the response and lead to a reduction in κ_L. In addition, the moment in the post-limit load response drops at a much faster rate [limit load indicated by (▲)]. (The limit load of the shell which exhibits localization occurs at a curvature which is somewhat lower than that in the uniformly rippled shell. This is due to the slightly larger overall amplitude of the imperfection used in the region of $s = 0$ as a result of the additional effect of a_i.) The second bifurcation is now seen to occur much earlier which may enable us to consider it as the cause of the catastrophic collapse observed in the experiments.

Predictions obtained from this analysis for $a_{0_i} = 10^{-3}$ and $a_i = 10^{-4}$ are compared to the experimental results in Fig. 11. The agreement between experiment and predictions is very good. The limit load is seen to occur very close to the curvature at which the shell collapsed (actual value of predicted limit load depends on the assumed amplitude of imperfections). The second bifurcation follows soon after the predicted limit load. In this analysis, the bifurcation check was applied to the central half wave which exhibits accelerated growth of ovalization. The ovalization predicted to occur in the crest of the localized region is also in good agreement with the ovalization measured in the experiment.

The progressive development of localized deformations in this shell is more clearly illustrated in Fig. 12, which shows the ovalization predicted along the length of the shell analyzed at different values of curvature. The axial ripples are seen to grow uniformly up to the limit load, beyond which the central part of the shell ovalizes faster. Figure 13 shows a graphical reproduction of a deformed configuration of the shell analyzed, which illustrates the non-uniform growth of the amplitude of the axial ripples. The central ripple is seen to grow significantly more than the others (localization). It is of interest to compare and observe the similarity of this picture with the experimental results shown in Fig. 9′.

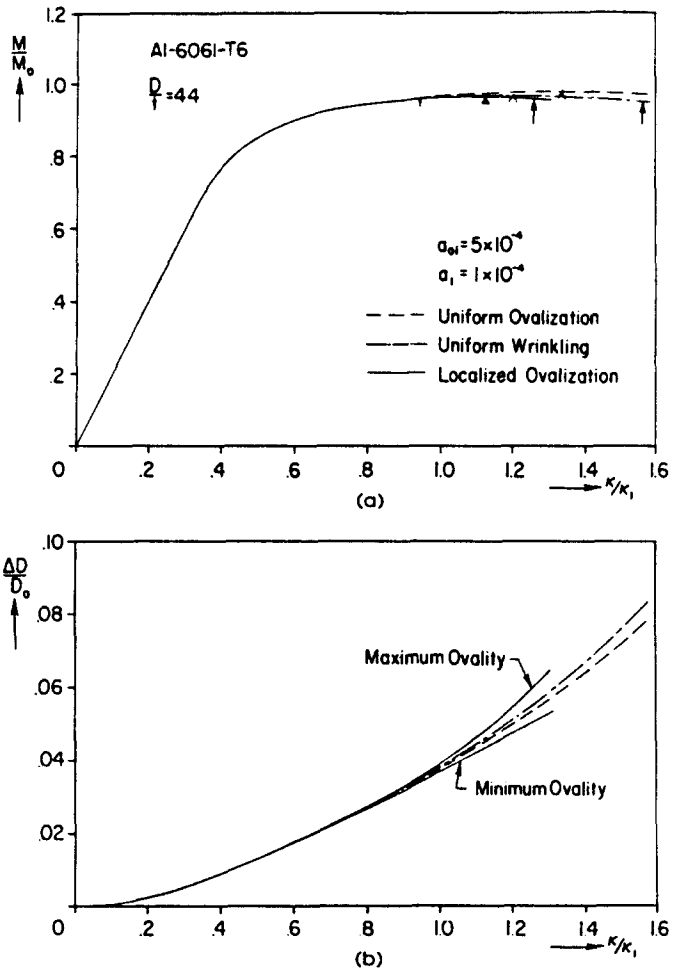

Fig. 10. Comparison of responses from three types of analyses ($D/t = 44$): (a) moment curvature; (b) ovalization curvature.

The effect of imperfection amplitude, a_{0i}, on the response of the structure is re-examined using the analysis which allows for localization of the axial ripples. Results for $a_{0i} = 0.5$, 1.0 and 3.0×10^{-3} are shown in Fig. 14 with a_i kept constant. As a_{0i} is increased, the value of the limit moment remains relatively unaffected but it occurs at progressively smaller values of curvature. The values of κ_L are similar to those shown in Fig. 8 for the uniformly rippled shell. The post-limit load moment is seen to drop more precipitously than in the corresponding results in Fig. 8. In all cases shown in Fig. 14, the second bifurcation occurs soon after the limit load, which is a distinct difference between the localized and uniform ripple results. The formulation used in this study assumes that rotations of the normals are moderate. Thus, significant excursions into the post-limit load regime will require higher order shell kinematics and, at a later stage, finite deformation constitutive models.

Figure 15 shows a set of predictions obtained with this analysis for a shell with $D/t = 60.5$. The experimental results are included for comparison purposes. The imperfection amplitudes used are again $a_{0i} = 10^{-3}$ and $a_i = 10^{-4}$. The major characteristics of the predicted results are the same as those of the previous shell analyzed. However, in this case, the second bifurcation is seen to occur very soon after the limit load. If we accept that this is responsible for the collapse of the structure, the closeness of the two instabilities explains the fact that in the experiments on this shell, the axial ripples were never seen to develop. The shell buckled suddenly and catastrophically.

The results presented above demonstrate the complexity of the deformation of the shell in the post-buckling regime. The sequence of critical events which occur during the loading

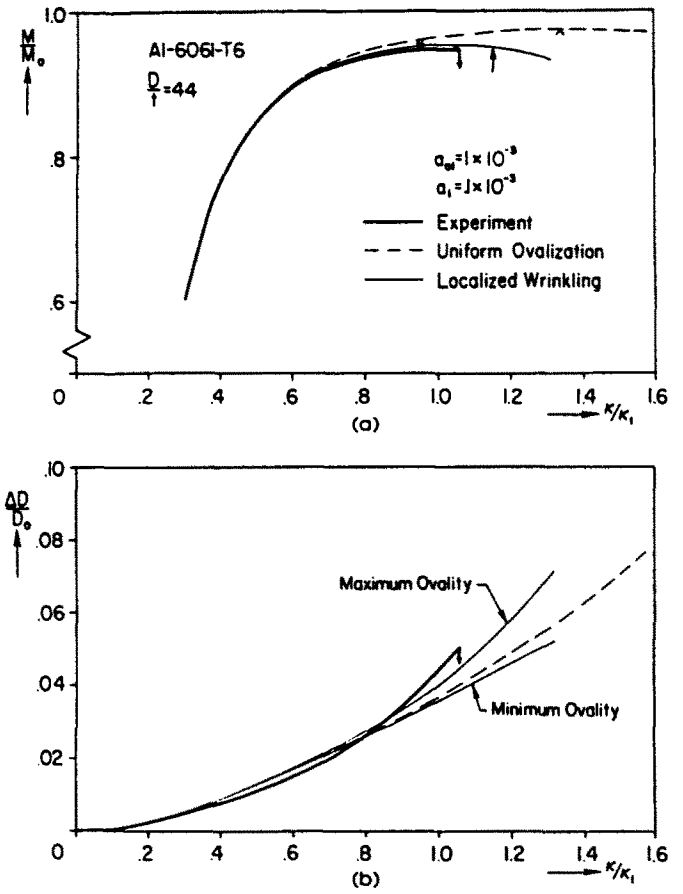

Fig. 11. Detailed comparison of experiment and predictions from analysis which includes ripple localization ($D/t = 44$).

history can be summarized as follows:

(a) Initially, the shell exhibits uniform ovalization, which grows non-linearly with curvature.

(b) At a curvature κ_b, the shell bifurcates at an increasing moment. The buckling mode consists of axially periodic ripples on the compressed side of the shell.

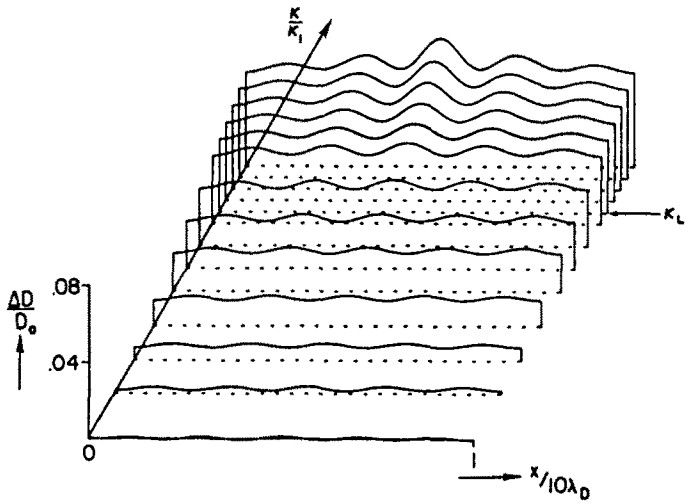

Fig. 12. Ovalization along the length as a function of curvature (illustrates localization of axial ripples).

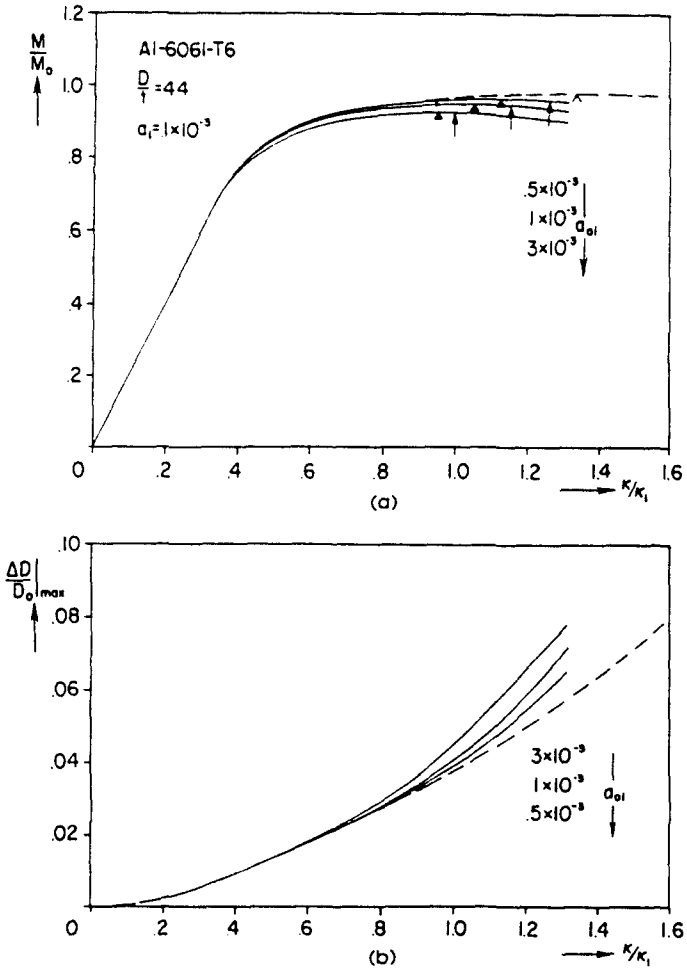

Fig. 14. Shell response as a function of imperfection amplitude ($D/t = 44$): (a) moment-curvature; (b) ovalization curvature.

(c) The amplitude of the ripples at first grows uniformly along the length. The net effect is a reduction in the rigidity of the shell, which results in the development of a load maximum.
(d) This limit load occurs at a curvature which is significantly smaller than that corresponding to the natural limit load instability inherent to the problem.
(e) Following the limit load, the ripples localize and the moment drops more precipitously.
(f) A second bifurcation was detected to occur in the ripple with the most severe deformation. This buckling mode is characterized by a number of circumferential waves.
(g) The second bifurcation and the relatively compliant nature of the pre-buckling response prior to it, are responsible for the localized catastrophic collapse observed in the experiments.
(h) In practice, ever present small geometric imperfections, which correspond to the two buckling modes of the problem, will be amplified in the neighborhood of the bifurcation points calculated, with equally catastrophic results as those described above.

(6) *Natural limit load and localization*

The behavior of thicker shells has been shown, in the experimental part of the study, to be governed by the natural limit load instability inherent to the problem. This class of

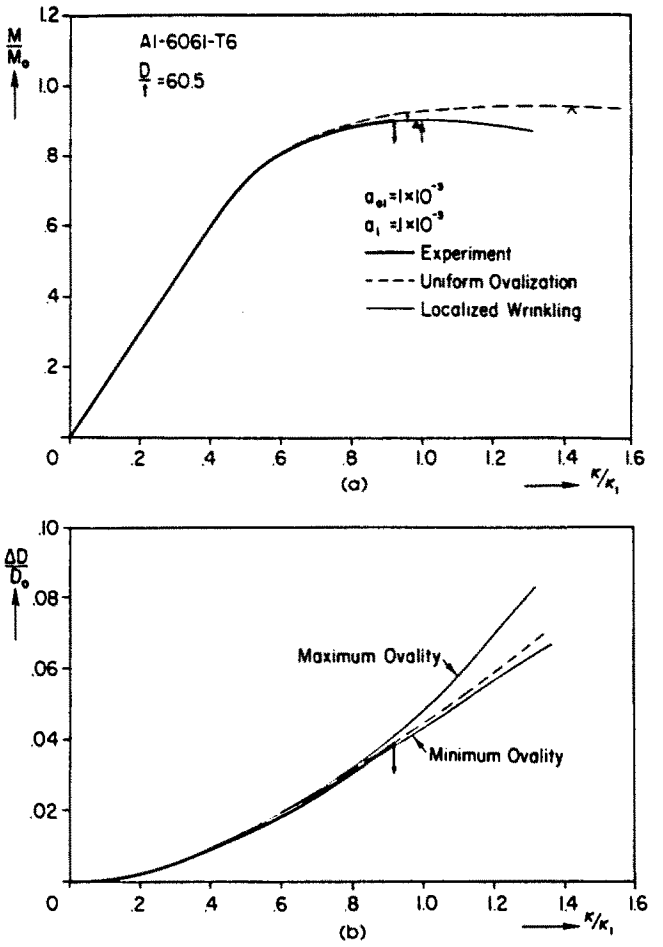

Fig. 15. Detailed comparison between experiment and predictions from analyses which include ripple localization ($D/t = 60.5$): (a) moment curvature; (b) ovalization curvature.

shells was found to ovalize quite uniformly up to approximately the limit moment beyond which the ovalization localized in a region a few shell diameters long. As the localization develops, the curvature of the shell starts to vary along the length. Thus the formulation of the problem presented in eqns (1)–(5) was generalized to include the case of $\kappa = \kappa(s)$. In addition, the length of the shell analyzed was increased (typical value used $L/D = 9.6$) to accommodate the length of the localized region observed in the experiments.

An approximate solution to the problem was obtained by adopting the following expansion for the curvature:

$$\kappa(s) = \frac{\Phi^*}{L} + \sum_{k=1}^{K} \kappa_k \left[\exp -\beta\left(\frac{ks}{L}\right)^2 - g_k \right] \tag{25}$$

where $\Phi(L) = \Phi^*$ is the rotation of the shell at $s = L$ which was prescribed incrementally. κ_k are unknown coefficients evaluated in the numerical solution and g_k are constants given as follows:

$$g_k = \int_0^1 \exp -\beta(k\xi)^2 \, d\xi \tag{26}$$

[(25) with (26) imply that $\Phi(0) = 0 \,\forall\, \Phi(L)$].

In the results shown below, the shell was assumed to be free of initial imperfections. When eqn (25) is adopted in eqns (1)–(5) the displacement components $\mathbf{u}$ are measured from a shell with circular cross-section and whose axis is deformed to $\kappa = \kappa(s)$. The displacements were approximated with the expansions given in eqns (21) with $p = \pi/L$, $N_r = N_w = J_u = 6$ and $I_u = 8$. For the longer shells analyzed $K = 10$ and $\beta = 1$ were used. Forty-eight integration points in $s \in [0, L]$ were found to lead to a sufficiently accurate solution. In spite of the specialized nature of the formulation and solution procedure used these changes increased significantly the numerical demands of the problem. A Cray-XMP computer was used to conduct the numerical analysis.

The moment–curvature and ovalization–curvature responses predicted through this solution procedure for an aluminum shell with $D/t = 19.5$, are shown in Fig. 16 together with the corresponding experimental results. The solution is seen to coincide with that from the uniform (ovalization) analysis up to the limit load. Indeed the limit loads from the two solutions are indistinguishable.

After the limit load, the predictions from the two analyses differ significantly. The current analysis yields a moment which drops precipitously with increasing curvature. Correspondingly, after the limit load the values of ovalization predicted at the two extremes of the length of the shell analyzed (see inset in Fig. 16) grow in a distinctly different manner. At $s = 0$, the ovalization grows at a significantly accelerated rate where as at $s = L$, it stops growing and even experiences a small decay.

A clearer view of the way and extent to which the ovalization localizes can be seen in Fig. 17 which shows a plot of the calculated ovalization along the length of the shell at different values of end rotation Φ^*. The ovalization remains uniform along the length up

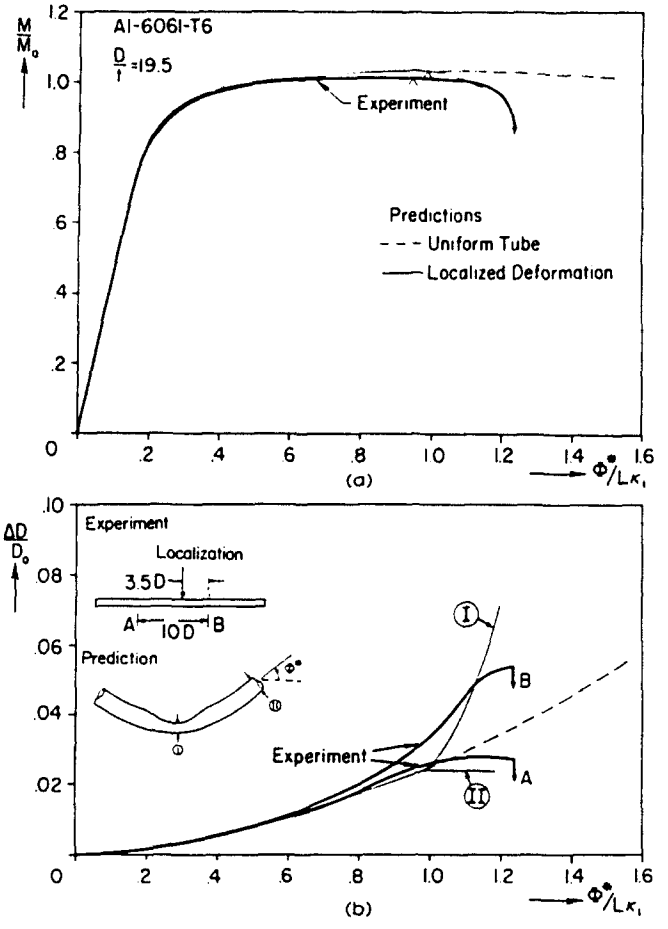

Fig. 16. Response of shell exhibiting natural limit load instability and localization ($D/t = 19.5$): (a) moment–curvature; (b) ovalization–curvature.

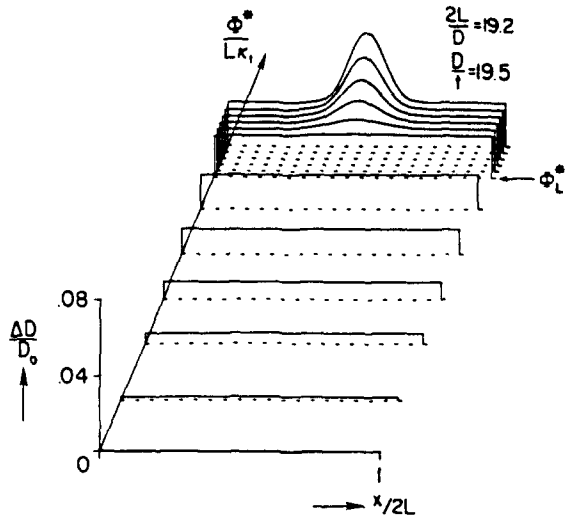

Fig. 17. Ovalization along length of shell at different values of Φ^*.

to the limit load (Φ_L^*). Further increase in Φ^* leads to localized growth of ovalization in the central region of the shell, whereas the ovalization away from the central section remains initially unchanged and decreases for higher values of Φ^*. The maximum ovalization is seen to grow to double the value in the uniform part of the shell with a relatively small increase in Φ^*. The results in this figure correspond to the experimental results shown in Fig. 23′ (excluding the extreme ends of the shell which in the experiment were constrained to remain circular due to the solid inserts used to apply the load). Indeed, the qualitative and quantitative similarity between the predicted and measured results is exceptionally good.

Figure 18 shows a graphical reproduction of the central part of a calculated deformed configuration in the post-limit load regime of the shell analyzed above (the length analyzed was 19.2D; the length shown is 14.4D). The nature of localization is quite clear and it compares quite well with the corresponding experimental results shown in Fig. 1d. It is important to note that, in the experiments, the localization will, in general, be triggered and occur in the region with the biggest imperfections (or at the ends, if the shell is improperly constrained). As a result, in any given experiment, the position of the localized region is more or less randomly located. The formulation used is such that localization is ensured to occur at mid-span (plane of symmetry). This, in general, does not affect the essence of the predicted results. It does, however, make a one-to-one quantitative comparison between the measured and predicted response after the limit load rather difficult, for the reasons explained in Part I. The case presented in Fig. 23′ is an exception, as the shell localized very close to mid-span.

Another problem whose behavior is governed by a natural limit load instability is that of inflation of a long tube which bulges in the neighborhood of the limit load. Kyriakides and Chang (1991) demonstrated that the post-limit load behavior of such a tube, and other structures belonging to the same family, is significantly influenced by the length of the structure. The main reason for this sensitivity is that, with the onset of localization, part of the structure continues to deform even though the load is dropping. At the same time, the part of the structure away from the region of localized deformation experiences unloading. Thus, the overall behavior is influenced by the ratio of the lengths of structure undergoing increasing and decreasing deformations.

The effect of the length of the shell on the calculated response of the present problem will be examined through an example involving an aluminum shell with $D/t = 25.3$. We first consider the response for a case with $2L/D = 25.6$. In order to illustrate the effect of localization on the behavior of the structure the *local* moment–curvature and moment–ovalization responses calculated at $s = 0$ and $s = L$ (identified as points I and II respectively) are compared in Fig. 19. The responses at the two points remain the same until the limit

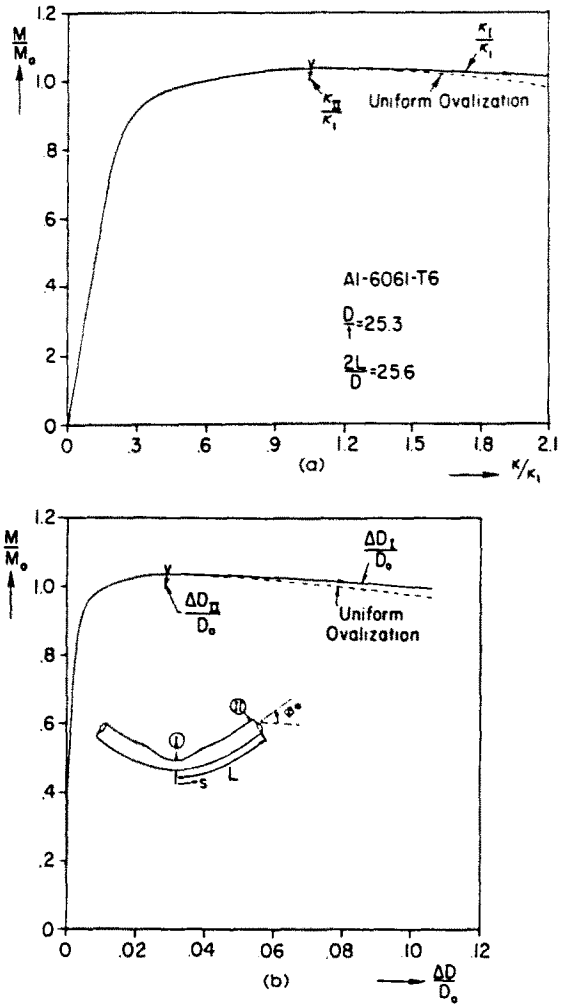

Fig. 19. (a) Moment curvature responses at points I and II. (b) Moment ovalization responses at points I and II.

moment is reached. Beyond the limit moment, the deformation in the mid-span area of the shell grows at a rate which is faster than that of the uniformly deforming shell. At the same time, the end of the shell starts to unload as shown in the figure. The unloading quickly becomes essentially elastic, indicated by the steep slope of the response at $s = L$ in both figures. The overall $M-\Phi^*$ and $\Delta D-\Phi^*$ responses of this shell are shown in Fig. 20. The post-limit load moment is seen to drop at a much faster rate than the uniformly ovalized shell.

Similar calculations were performed for two additional shells with lengths of $2L/D = 19.2$ and 12.8. The results are also included in Fig. 20. The moment–curvature and ovalization–curvature responses of the three shells are seen to be independent of the length up to the limit moment. Beyond the limit moment the deformations of all three shells localize as evidenced by the different ovalizations recorded at the mid-spans and at the ends of the shells. Figure 21 shows detailed plots of the ovalization along the length for the shells with $2L/D = 25.6$ and 12.8 for various values of $\Phi^* \geqslant \Phi^*_l$. The two sets of results shown were selected to have approximately the same values of maximum ovalizations (i.e. they correspond to different values of Φ^*). The length of the shell experiencing localization, in the deformation regime shown, is approximately nine diameters for both cases. In fact, the overall geometries of the localized regions of the three shells are very similar indeed. We thus conclude that the detailed deformation and the length of the localized region are governed primarily by local equilibrium and not by the overall length of the shell.

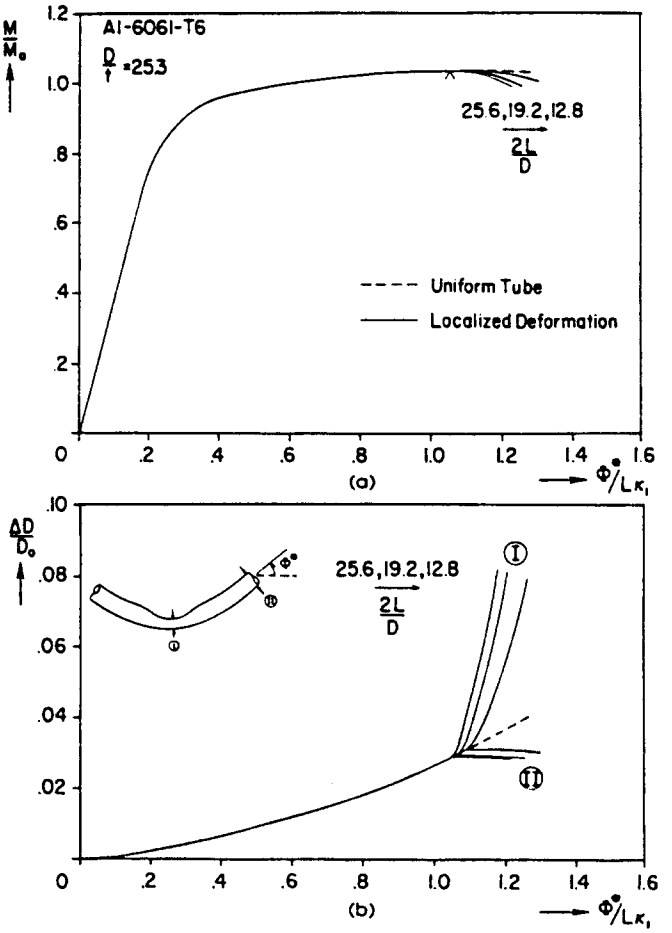

Fig. 20. Responses of shells of different length exhibiting limit load instability and localization: (a) moment curvature; (b) ovalization curvature.

However from Fig. 20a it can be seen that the overall post-limit load $M-\Phi^*$ response of the shell is significantly affected by the length of the shell. As the length of the shell increases the moment drops at a much faster rate with Φ^*. This has a corresponding effect on the deformation in the localized region as shown in Fig. 20b. This difference can be explained as follows. It has been shown that the length of the shell undergoing localization

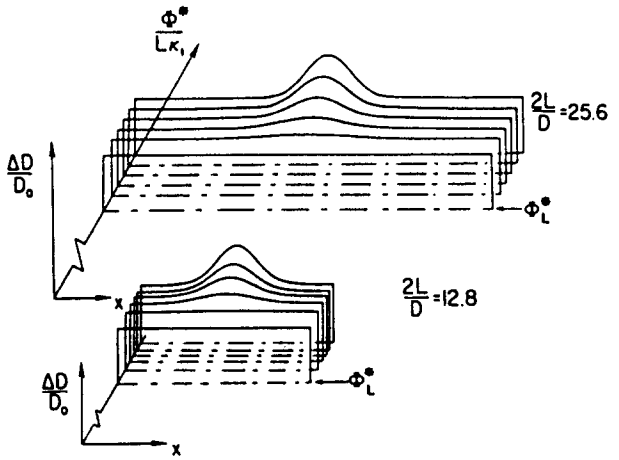

Fig. 21. Ovalization along length of shell at different values of $\Phi^* \geqslant \Phi^*_L$. Comparison between shells of length of 25.6 and 12.8 diameters.

is approximately the same for the three cases. Thus, the length of shell which remains uniform in the case with $2L/D = 25.6$ is longer than that with $2L/D = 12.8$. As the moment drops the uniform section(s) undergoes unloading even though the net end rotation increased. Thus, the increase of deformation in the localized region depends on the increase in the end rotation and on the amount of rotation caused by the unloading of the uniform section. For the longer shell, the second component is larger and, as a result, a smaller end rotation is required to deform the localized section.

In order to illustrate this point further, a series of additional shells with lengths of $2L/D = 51$, 102, 205 and 410 were analyzed in the following approximate fashion. The shell with length of 25.6 diameters is clearly long enough for the response of its ends to be assumed to be unaffected by the localized deformation which takes place at mid-span. Thus, the response of the end of this shell was assumed to be also representative of the response away from the localized region of longer shells. This simplification was used to calculate the $M-\Phi^*$ response of the long shells given above. The results are shown in Fig. 22. As L increases, the post-limit load response drops more precipitously. For very long shells, the $M-\Phi^*$ response turns backwards. Clearly, in such cases, even under curvature control conditions, the shell will fail catastrophically upon reaching the limit load by folding into two sections.

(7) *Behavior of shells with intermediate D/t values*

In the experimental part of this study it was shown that aluminum 6061-T6 shells with $28 < D/t < 40$ exhibited rather complex behavior which involved short wave ripples as well as localized deformation which extended over a length of a few shell diameters. The ratio of the characteristic lengths of the two events was approximately 20. Thus numerical modelling of the problem became more cumbersome. The formulation presented in eqns (1) (5) was used to approximately analyze a shell with half length of $L/D = 9.6$ and $D/t = 35.7$. The shell was assumed to have an initial geometric imperfection as follows:

$$\bar{w} = -R\left[a_i \cos\frac{\pi s}{\lambda_D}\exp -\beta\left(\frac{s}{5\lambda_D}\right)^2 + \bar{a}_i \cos\frac{\pi s}{l}\exp -\beta\left(\frac{s}{l}\right)^2\right]. \tag{27}$$

For the case analyzed $l = 3.2D$ was used. The shell was discretized through the following series expansions for the displacements:

$$u = R\sum_{i=1}^{I_u}\sum_{j=0}^{J_u} c_{ij}\sin\frac{i\pi s}{L}\cos j\theta + R\sum_{i=1}^{\bar{I}_u}\sum_{j=0}^{\bar{J}_u}\bar{c}_{ij}\sin\frac{i\pi s}{5\lambda_D}\exp -\beta\left(\frac{s}{5\lambda_D}\right)^2\cos j\theta$$

$$v = R\sum_{n=2}^{N_v} b_n \sin n\theta + R\sum_{i=1}^{I_v}\sum_{j=1}^{J_v} d_{ij}\cos\frac{i\pi s}{L}\sin j\theta + R\sum_{i=1}^{\bar{I}_v}\sum_{j=1}^{\bar{J}_v}\bar{d}_{ij}\cos\frac{i\pi s}{5\lambda_D}\exp -\beta\left(\frac{s}{5\lambda_D}\right)^2\sin j\theta$$

$$w = R\sum_{n=0}^{N_w} a_n\cos n\theta + R\sum_{i=1}^{I_w}\sum_{j=0}^{J_w} e_{ij}\cos\frac{i\pi s}{L}\cos j\theta$$

$$+ R\sum_{i=1}^{\bar{I}_w}\sum_{j=0}^{\bar{J}_w}\bar{e}_{ij}\cos\frac{i\pi s}{5\lambda_D}\exp -\beta\left(\frac{s}{5\lambda_D}\right)^2\cos j\theta. \tag{28}$$

The curvature $\kappa(s)$ was again represented through expressions (25) and (26). The following number of terms were used in the series expansions above: $N_u = I_u = J_u = 6$, $\bar{I}_u = \bar{J}_u = 8$ and $K = 5$. Ninety integration points in $s \in [0, L]$ were used and distributed unevenly along the length. The problem was again solved by prescribing the end rotation Φ^*. The amplitudes of the initial imperfections used were $a_i = 0.5 \times 10^{-3}$ and $\bar{a}_i = 0.5 \times 10^{-3}$. The nature of the imperfections as well as the displacement functions adopted allow the growth, localization and possibly the interaction of short wavelength ripples and long wavelength instabilities. A set of results are shown in Fig. 23. The results from the uniformly deformed shell are included for comparison purposes. The presence of the small imperfections has relatively little effect on the predicted response up to the first bifurcation point (indicated by "↑"). In the neighborhood of the bifurcation point the amplitude of the short wavelength ripples

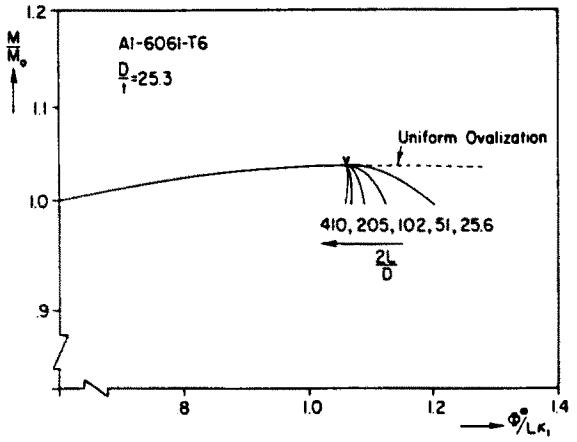

Fig. 22. Moment–curvature responses of shells with different lengths.

start to grow. The bias provided in the imperfection is amplified and the growth of the ripples localizes. This is demonstrated in Fig. 24 in which the ovalization along the shell length is plotted for various values of end rotation Φ^*. A moment maximum develops and the shell response starts to decay precipitously. Prior to the limit moment a second localization phenomenon which involves a few diameters of the shell on either side of the rippled section is seen to occur in Fig. 24. This is similar in nature to what was observed experimentally in Fig. 17[7]. As in the case of the thinner shells analyzed earlier a second

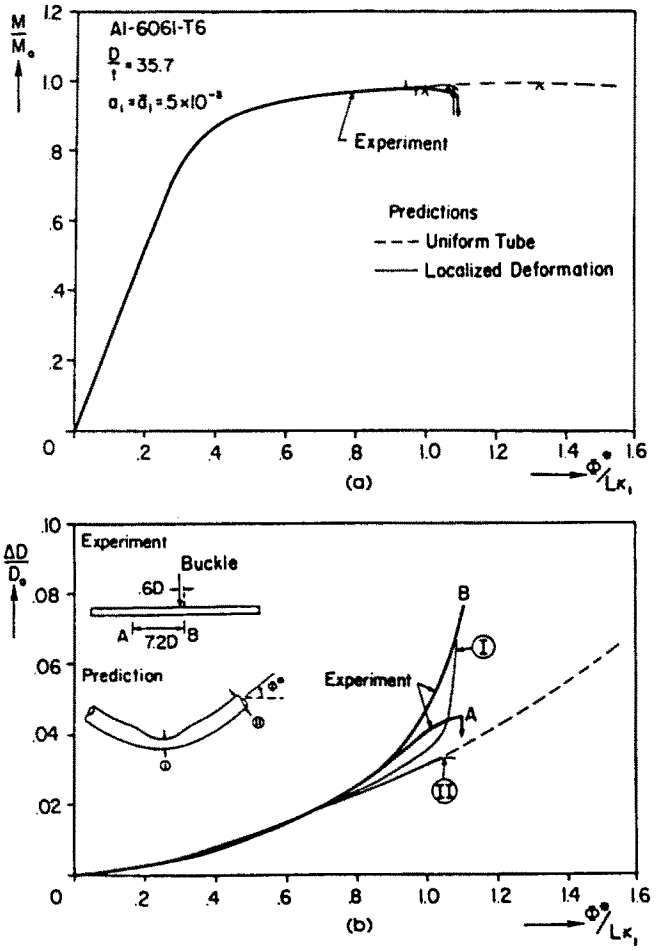

Fig. 23. Response of shell with $D/t = 35.7$: (a) moment–curvature; (b) ovalization–curvature.

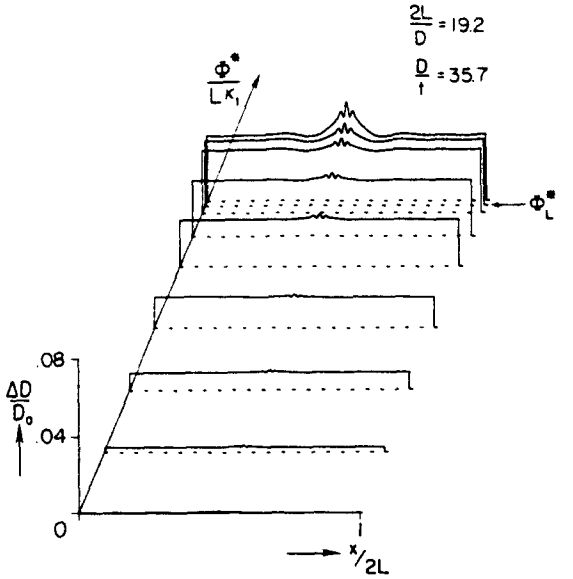

Fig. 24. Ovalization along length of shell at different values of Φ^*.

bifurcation point was identified in the largest of the short wavelength ripples soon after the limit moment as shown in Fig. 23. This is again similar qualitatively at least to the experimental results. The limit load predicted is seen to occur at a much smaller curvature than that predicted for the uniformly ovalized shell. Quite clearly the rotation Φ_L^* corresponding to this limit load should be considered as the maximum allowable value for such shells.

The results presented indicate that short wave ripples are again the triggering mechanism for the sequence of events that follow their onset.

Acknowledgements—The authors benefitted from discussions of the problem with J. W. Hutchinson and M. Stern. The work presented was conducted with financial support from the U.S. Office of Naval Research under contract N00014-88-K-0610.

REFERENCES†

Batdorf, S. B. (1949). Theories of plastic buckling. *J. Aero. Sci.* **16**, 405–408.
Bushnell, D. (1974). Bifurcation buckling of shells of revolution including large deflections, plasticity and creep. *Int. J. Solids Structures* **10**, 1287–1305.
Christoffersen, J. and Hutchinson, J. W. (1979). A class of phenomenological corner theories of plasticity. *J. Mech. Phys. Solids* **27**, 465–487.
Gellin, S. (1976). Buckling of cylindrical shells in the plastic range. Ph.D. Thesis, Harvard University, Cambridge, MA.
Koiter, W. T. (1963). The effect of axisymmetric imperfections on the buckling of cylindrical shells under axial compression. *Pro. Kon. Ned. Ak. Wet.* **B66**, 265–279.
Kyriakides, S. and Chang, Y. C. (1991). On the initiation and propagation of a localized instability in an inflated elastic tube. *Int. J. Solids Structures* **27**, 1085–1111.
Needleman, A. and Tvergaard, V. (1982). Aspects of plastic post-buckling behavior. In *Mechanics of Solids*, The Rodney Hill 60th Anniversary Volume (Edited by H. G. Hopkins and M. J. Sewell), pp. 435–498. Pergamon Press, Oxford.
Tvergaard, V. (1983). On the transition from a diamond mode to an axisymmetric mode of collapse in cylindrical shells. *Int. J. Solids Structures* **19**, 845–856.
Tvergaard, V. and Needleman, A. (1980). On the localization of buckling patterns. *ASME J. Appl. Mech.* **47**, 613–619.

† Additional references listed in Part I.

APPENDIX A

The metric and curvature tensors of a circular cylindrical shell of radius R with an initial geometric imperfection given by $\bar{w} = \bar{w}(s, \theta)$ are as follows:

$$\bar{a}_{\alpha\beta} = \begin{bmatrix} 1 + \bar{w}_{,s}^2 & \frac{1}{R}\bar{w}_{,s}\bar{w}_{,\theta} \\ \frac{1}{R}\bar{w}_{,s}\bar{w}_{,\theta} & 1 + \frac{2\bar{w}}{R} + \frac{\bar{w}_{,\theta}^2}{R^2} \end{bmatrix}, \tag{A1}$$

$$\bar{b}_{\alpha\beta} = \begin{bmatrix} -\bar{w}_{,ss} & -\frac{1}{R}\bar{w}_{,s\theta} \\ -\frac{1}{R}\bar{w}_{,s\theta} & \frac{1}{R}\left(1 - \frac{1}{R}\bar{w}_{,\theta\theta}\right) \end{bmatrix}. \tag{A2}$$